







Original Article

Comparison of DEM accuracies generated from different stereo pairs over a plateau mountainous area

LIU Han-hu*  <https://orcid.org/0000-0002-2928-7995>;  e-mail: liuhanhu@qq.com

ZHAO Yin-jun*  <https://orcid.org/0000-0002-0111-3694>;  e-mail: crpp0104@163.com

WANG Lei¹  <https://orcid.org/0000-0003-3837-9629>; e-mail: 576210903@qq.com

LIU Yan-yan¹  <https://orcid.org/0000-0002-4414-2786>; e-mail: y_l147@txstate.edu

*Corresponding author

¹ College of Earth Sciences, Chengdu University of Technology, Chengdu 610059, China

² Key Laboratory of Environment Change and Resources Use in Beibu Gulf, Ministry of Education, Guangxi Teachers Education University, Nanning 530001, China

Citation: Liu HH, Zhao YJ, Wang L, et al. (2021) Comparison of DEM accuracies generated from different stereo pairs over a plateau mountainous area. *Journal of Mountain Science* 18(6). <https://doi.org/10.1007/s11629-020-6274-1>

© Science Press, Institute of Mountain Hazards and Environment, CAS and Springer-Verlag GmbH Germany, part of Springer Nature 2021

Abstract: Digital elevation models (DEMs) can be quickly and conveniently generated using very high resolution (VHR) satellite stereo images. Previous studies have evaluated and compared DEM accuracy based on VHR satellite stereo pairs collected by different satellite sensors. However, few studies analyzed the accuracy of a DEM based on stereo image pairs from a satellite with the same orbit and different orbits for a region with significant topographic fluctuations in the plateau area. Referring to former studies, this paper had two objectives: to generate a digital elevation model (DEM) and evaluate its horizontal and vertical accuracy over a plateau area with high relief; and to study the mapping capability of multiorbit and multitemporal stereo pair images in the plateau mountainous region. To achieve these objectives, we collected the 2015 Worldview-2 stereo image pair and another three WorldView-2 images acquired in 2013, 2014, and 2015. First, the 2015 DEM was

obtained using a strict physical model based on along-track stereo image pairs, and the reliability of the DEM was verified with field data. Then, the images obtained in 2013, 2014, and 2015 were combined into different-orbit stereo image pairs, DEMs were produced using rational function models, and the DEMs were verified using field data and the 2015 DEM as standards. The results showed that the relief degree has a particular influence on the DEM, and the precision of the DEM decreases as the topographic relief increases. Off-nadir angles can also influence DEM accuracy, with a larger angle corresponding to a lower DEM accuracy. The research also shows that the DEM obtained from four sets of experiments meets the accuracy requirement of a 1:5,000 digital elevation map, digital line graphic (DLG), and digital orthophoto map (DOM). Among these four groups of DEMs, the one based on the 2015 stereo pairs with the same satellite achieved the highest precision.

Received: 27-Jun-2020
1st Revision: 18-Jan-2021
2nd Revision: 20-Mar-2021
Accepted: 30-Mar-2021

Keywords: Remote sensing; Worldview; Satellite images; Digital elevation model; Photogrammetry

1 Introduction

High-precision digital elevation models (DEMs) are basic requirements for constructing regional maps, and they can be obtained using a variety of techniques, such as traditional ground measurement techniques, e.g., GNSS (Global Navigation Satellite System) surveys, total station surveys, etc., and photogrammetry and remote sensing technologies that rely on different platforms and different sensors, such as interferometric synthetic aperture radar (InSAR) images, light detection and ranging (LiDAR) technology, unmanned aerial vehicles (UAV) surveys, and high-resolution satellite stereo imagery. On plateau mountainous area, traditional field topographic surveys are impossible. The DEM accuracy from InSAR is challenging to guarantee due to geometric problems (such as perspective shrinkage, overshadowing, and shadowing), changes in atmospheric conditions, and incorrect baseline estimates (Muskett et al. 2008, Zhu et al. 2018); LiDAR is difficult to implement widely due to the requirement for aerial flight measurements (Goulden et al. 2016, Vassilaki and Stamos 2020); and UAVs are greatly affected by weather and difficult to implement in large areas with plateaus and mountains and have high costs (Uysal et al. 2015, Akturk and Altunel 2019). With the rapid development of satellite stereo mapping technology, exceptionally high resolution (VHR) satellite stereo pairs have become one of the leading technologies for obtaining DEMs on a large scale (Shean et al. 2016, Nemmaoui et al. 2019). For example, the DigitalGlobe company produced the entire Arctic DEM (<https://www.pgc.umn.edu/data/arcticdem/>) based on Worldview-1, Worldview-2, and Worldview-3 optical stereo imagery, and the details have been previously described (Noh and Howat 2015).

The derivation of a DEM from VHR satellite stereo images has until now been possible using imagery from IKONOS (Fraser et al. 2002a, 2002b, Bang et al. 2003), GeoEye (Fraser and Ravanbakhsh 2009), Quickbird (Noguchi et al. 2004), Pleiades-1/2 (Lacroix 2015, Poli 2015), and Worldview1/2/3/4 (Toutin 2012, Reinartz et al. 2014). For these VHR satellite stereo images, due to the high on-orbit height of the sensor and the relatively small image size, the field of view of the image is minimal (DigitalGlobe 2010), which prevents the application of a fixed tilt angle when shooting high-scoring images; thus, image

acquisition will be restricted. Since most VHR satellite stereo imagery is obliquely photographed, an image projection difference is caused by the image's tilt. In mountainous areas (with a height difference of nearly 2 km within a few kilometers of the study area), terrain projections will inevitably be caused by terrain elevations. The procedure for assessing DEM quality involves an examination of the horizontal and vertical accuracy (Nemmaoui et al. 2019). Therefore, one of the objectives of this paper is to produce a digital elevation model and evaluate its horizontal and vertical accuracy.

Many VHR satellite sensors have formed satellite groups to suppress stereo mapping. Such satellite groups, which have the advantages of a large angle and effective attitude control, can perform earth observations using both the same and different orbits (Toutin and Cheng 2001). Many studies have focused on along-track satellite production of DEMs (Shaker et al. 2010, Saldaña et al. 2012, Zhou 2015, Wang et al. 2019). Shaker (Shaker et al. 2010) proved that the feature accuracy based on IKONOS stereo pair extraction is within one pixel. Saldaña et al. (2012) applied GeoEye-1 stereo pairs for DEM extraction and analysis, and the results showed that the planimetric and vertical accuracy of the DEM was better than 0.5 m. Zhou (Zhou et al. 2015) applied Pleiades to extract a DEM with an elevation accuracy of 0.3 m. Wang (Wang et al. 2019) showed that the average elevation error of DEMs extracted by applying WorldView-2 was 0.57 m. Existing research shows that the accuracy of the DEM from the same orbit is reliable. Although DEMs generated from multiorbit stereo pairs have been investigated (Giribabu et al. 2013, Bagheri et al. 2018), further studies are required to determine the effective use of multiorbit stereo pairs (Poli et al. 2015); moreover, few studies have focused on stereo pairs acquired by the same satellite at different times and in different orbits. Thus, the second goal of this paper is to study the mapping capability of multiorbit and multitemporal stereo pair images.

This paper collected the 2015 WorldView-2 stereo image pair and three other WorldView-2 images (acquired in 2013, 2014, and 2015) to achieve the above two goals. First, the 2015 DEM was obtained using a strict physical model based on along-track stereo image pairs, and the reliability of the DEM was verified with field data. Then, the images acquired in 2013, 2014, and 2015 were combined into three sets of stereo pairs, DEMs were produced using

rational function models, and the DEMs were verified using field data and the 2015 DEM as standards.

2 Study Area and Data

2.1 Study area

The study area was Nuomuhong County, Qinghai Province, China. The terrain in the area includes steep and dangerous mountains, and the elevation ranges from 2884 m to 4644 m. The lithology is exposed, and the vegetation cover is minimal, and the mountain slopes are mostly greater than 30°. The area is not easily accessible, and the working conditions are poor; therefore, this region is well suited for obtaining DEMs using stereo pairs.

2.2 Datasets

2.2.1 Satellite imagery

In this paper, we first acquired Worldview-2 along-track satellite images of the research area on July 10, 2015. The data product type is a Stereo1B image (DigitalGlobe 2020), which is one of DigitalGlobe’s Basic imagery products, which have basic radiometric and sensor corrections but no geometric corrections. These basic products are similar to raw images and among the least corrected products in DigitalGlobe’s satellite imagery. These products include image support data (ISD) files, which contain full information about the attitude and ephemeris data, geometric calibration, camera models, and rational polynomial coefficients. Clouds cover the data product in the southeast corner, making it difficult to produce DEMs in this area. Therefore, three Worldview-2 ORS2A images obtained on May 25, 2013, May 16, 2014, and July 24, 2015 were subsequently purchased. The ORS2A images have been radiometrically and geometrically corrected (DigitalGlobe 2020), and they are georeferenced to a cartographic projection using a constant height surface and include the corresponding rational function model (RFM) sensor and a metadata file. The spatial relationship of each image is shown in Fig. 1, and the satellite data parameters are shown in Table 1.

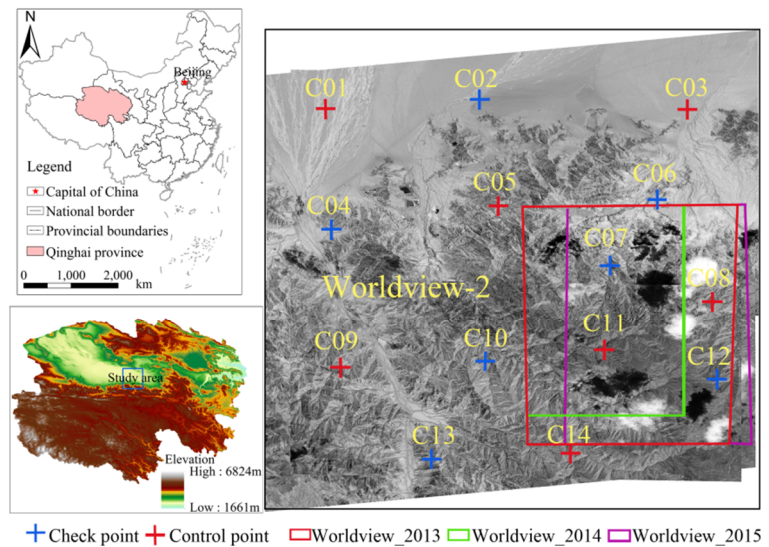


Fig. 1 Location of the study area: Nuomuhong County, Qinghai Province, China.

2.2.2 Ground point collection

For field control point acquisition, a Zhonghaida V30 GPS receiver was used. The device has 12 channels, the measurement phasor is L1, the carrier phase is L2, and the memory is 64 MB. Its horizontal accuracy is 5 mm + 1 ppm × D, and its elevation accuracy is 10 mm + 1 ppm × D, where D is the measured distance in km.

In this paper, three national third-level traverse points and three third-level level points from the Tibet Bureau of Surveying and Mapping were collected in terms of basic control data. The traverse points are the results of the 1980 Xi’an coordinate system, and the results are converted into 3° zone results. The third-level level is the 1985 National Height Datum. This project’s control survey initially performs the C-level GPS network measurement and then the E-level GPS image control point measurement based on the C-level GPS results.

When selecting control points and checkpoints in the field, we need to choose locations that are obvious and clear in the image and are easy to accurately locate and measure in the field, as shown in Fig. 2.

3 Methodology

The basic theory of using satellite remote sensing stereo pairs to obtain DEMs is that satellites need to obtain images of the same place from two different angles (Wang et al. 2019). We establish 3D

Table 1 Image data parameters for the different time periods used in this study.

Acquisition date	2015-07-10	2015-07-10	2013-04-25	2014-05-16	2015-07-24
Image Type	Worldview-2 Stereo1B	Worldview-2 Stereo1B	Worldview-2 ORS2A	Worldview-2 ORS2A	Worldview-2 ORS2A
LL Long. and LL Lat. (°)	95.844365 36.152148	95.832635 36.132800	95.943242 36.269172	95.943199 36.268038	95.671899 36.324319
UR Long. and UR Lat. (°)	96.037284 36.319787	96.046395 36.346432	96.040424 36.266739	96.018156 36.266168	95.919758 36.370485
UL Long. and UL Lat. (°)	95.845242 36.323297	95.836244 36.326349	96.036197 36.157502	96.014513 36.171334	95.676147 36.197256
LR Long. and LR Lat. (°)	96.035784 36.150113	96.039641 36.150294	95.939150 36.159926	95.939646 36.173197	95.923486 36.243858
Off-Nadir View Angle	17.8	24.5	18.0	4.9	33.1
Scan Direction	Forward	Forward	Forward	Reverse	Forward
Collected Row GSD	0.518 m	0.562 m	0.489 m	0.474 m	0.644 m
Collected Column GSD	0.491 m	0.539 m	0.522 m	0.466 m	0.654 m
Mean Product GSD	0.516 m	0.553 m	0.505 m	0.470 m	0.649 m
Solar Azimuth (°)	130.4	131.3	160.8	145.1	126.5
Solar Altitude (°)	70.4	70.6	66.1	70.1	65.9
Satellite Azimuth (°)	350.0	210.5	262.0	39.6	40.3
Satellite Altitude (°)	70.2	62.1	69.6	84.7	52.5

Note: For the abbreviations in the first column, LL, UR, UL, LR refer to the lower left, upper right, upper left, and lower right, respectively. Long., Longitude; Lat., Latitude. GSD denotes ground sample distance.

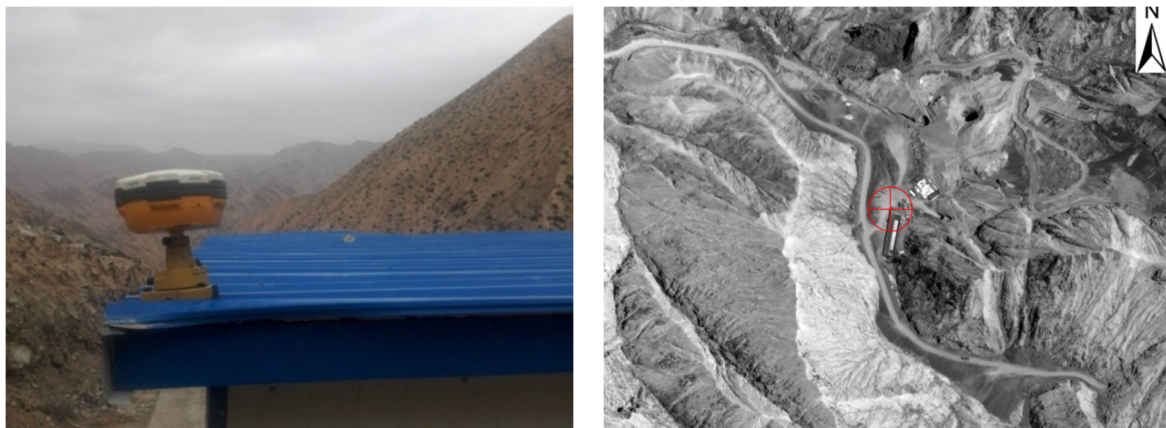


Fig. 2 Field collection points and the corresponding images.

coordinates by linking the same place on the two images and further build an actual ground stereo model based on the ground control points. This paper presents a bundle-based block adjustment method based on a strict geometric model for high-resolution remote sensing images that use minimal control points. The method uses collinearity equations as basic equations and then acquires exterior orientation elements of two stereo pairs with the along-track or multiorbits and coordinates of the ground (Poli and Toutin 2012). Block adjustments using the bundle method effectively obtain a high-precision positioning model using two image join points and field control points (Toutin 2011). It is assumed that S is the center of the image and M is a certain object on the Earth's surface. The coordinates of surface object M on the

image plane coordinate system, image space auxiliary coordinate system, and world coordinate system are (x, y) , (X_m, Y_m, Z_m) , and (X, Y, Z) , respectively. The coordinates of S on the world coordinate system are (X_s, Y_s, Z_s) . According to the collinear condition, M , S , and the image point of M have the following relationship:

$$\frac{X_M}{X-X_S} = \frac{Y_M}{Y-Y_S} = \frac{Z_M}{Z-Z_S} = \lambda \tag{1}$$

According to the relationship between the image plane coordinates and the image space auxiliary coordinates, the collinear equation can be obtained as follows:

$$x-x_o = -f \frac{a_1(X-X_S)+b_1(Y-Y_S)+c_1(Z-Z_S)}{a_3(X-X_S)+b_3(Y-Y_S)+c_3(Z-Z_S)} \tag{2}$$

$$y-y_o = -f \frac{a_2(X-X_S)+b_2(Y-Y_S)+c_2(Z-Z_S)}{a_4(X-X_S)+b_4(Y-Y_S)+c_4(Z-Z_S)} \tag{3}$$

Table 2 Different schemes used in this study.

Scheme name	Image type	Imaging time	Orbit
Scheme A	Stereo1B	2015.7.10 and 2015.7.10	Same orbit
Scheme B	ORS2A	2013.4.25 and 2014.5.16	Different orbit
Scheme C	ORS2A	2013.4.25 and 2015.7.24	Different orbit
Scheme D	ORS2A	2014.5.16 and 2015.7.24	Different orbit

where x_o , y_o and f are the elements of interior orientation. Through linearization of the collinear equation, an error equation and exterior orientation elements can be obtained. Finally, the ground coordinates are obtained through a forward intersection.

The five Worldview-2 panchromatic channel remote sensing images are used to generate combinations of four different satellite stereo image pairs, from which the DEM design is extracted. Information on these combinations is shown in Table 2.

This article designs an experimental technology diagram based on combining the above four groups of stereo image pairs, as shown in Fig. 3. First, the 2015 DEM was obtained using a strict physical model based on along-track stereo image pairs, and the reliability of the DEM was verified with field data. The images obtained in 2013, 2014, and 2015 were combined into different-orbit stereo image pairs. Finally, the DEM was produced using rational function models and verified using field data and the 2015 DEM as

standards. The Erdas 2015 Leica Photogrammetry Suite (LPS) platform was used for data processing and analysis to carry out relative orientation, absolute orientation, automatic matching of tie points, and aerial triangulation. The major steps are illustrated as follows (Fig. 3).

3.1 Relative orientation

After importing different off-nadir view angle images, we need to create a pyramid model and carry out interior orientation based on the sensor model. Sensor modeling for remote sensing image data can be defined as a procedure that establishes the geometric relationship between the object and image coordinates (Jeong and Kim 2015). Appropriate sensor models are required to implement accurate geopositioning from satellite stereo pairs. Sensor models for satellite imagery can be categorized into rigorous sensor models (RSMs) and rational function models (RFMs). According to previous studies (Jeong and Kim 2015, Shean et al. 2016), the precision of the plane coordinates and elevation coordinates of DEMs obtained based on rigorous sensor models are relatively stable and higher. However, the stereo pair image with the rigorous model is more expensive. Therefore, this experiment designed Scheme A using the rigorous sensor model and Scheme B, Scheme C, Scheme D using the rational function model.

3.2 Absolute orientation

Absolute orientation transfers field control point data to the corresponding position on the image. According to the experimental requirements, the control points need to be accurately positioned on each relevant image (Shean et al. 2016).

3.3 Automatically match tie points

The key to automatically generating encrypted points is to match the same position points obtained by two images. Image matching is based on the correlation between features, structures, textures, and gray levels

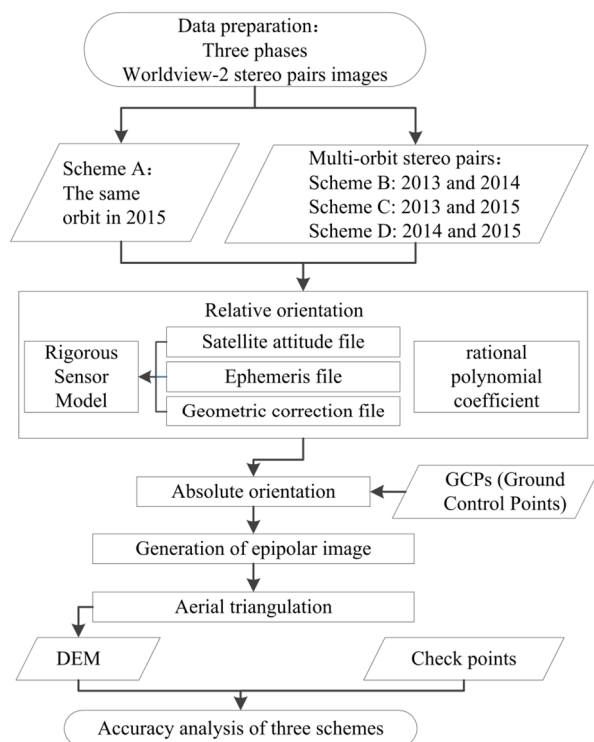


Fig. 3 Block diagram of the full process.

among images (Shean et al. 2016), and it represents the process of identifying two or more images in the same place through an algorithm. The process of LPS automatic matching at the same location mainly consists of three parts. First, multilevel matching of the pyramid is realized, and then terrain and geometric constraints are added to obtain high-precision connection points. Finally, least-squares matching is performed.

3.4 Aerial triangulation

Aerial triangulation is mainly based on the field control points, and it is performed to calculate the plane and elevation coordinates of the encrypted points (Shean et al. 2016). The median error of the aerial triangulation results in the LPS software must be less than 1 pixel. After aerial triangulation is completed, the digital elevation model of the image's overlapping area can be obtained by interpolating the automatically extracted encrypted points.

3.5 DEM generation

The LPS eATE module was used to generate the point cloud file and convert it into text format. Then, we used the continuous tension curvature spline interpolation method to generate the DEM.

4 Results and Discussion

4.1 DEM extraction from along-track stereo pairs

The two Worldview-2 images from 2015 (scheme A) belong to the same track stereo image pair, and the DEM is acquired based on a strict physical model. The DEM effect in some areas is shown in Fig. 4.

DEM accuracy is very important because accuracy directly affects the model's application in engineering construction. Although the planimetric and vertical accuracies of the DEM obtained based on rigorous sensor models are higher than those obtained based on rational function models, there are still many factors affecting its accuracy, including

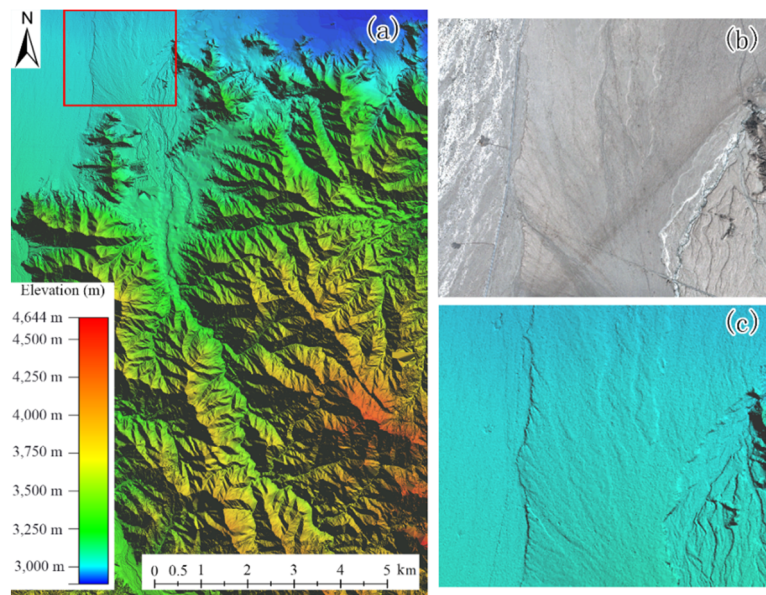


Fig. 4 a) DEM from 2015 VHR satellite stereo pairs. The red box represents the stereo image pair of the same track in the same area: b) VHR satellite image; c) DEM.

rigorous sensor models, image matching methods, and the number and distribution of GCPs (Ground Control Points) (Aguilar et al. 2013, Poli et al. 2015, Goldbergs et al. 2019). The terrain height difference in the study area is very large. According to the image point displacement law, as the terrain height difference becomes larger, the projection difference becomes larger. The projection difference caused by terrain fluctuations can be calculated by formula (4):

$$h = ctg \theta \times H \tag{4}$$

where θ is the imaging height angle of the sensor and H is the height of the ground feature. In this paper, the WorldView-2 imaging height angle is 56.9° and the projection difference h is calculated as follows:

$$h = ctg \theta \times H = ctg 56.9 \times H = 0.5294H$$

Therefore, in this scene image, the height difference of 10 m will produce a projection difference of 5.294 m (approximately 10 pixels). In previous DEM accuracy evaluation studies (Aguilar et al. 2013, D. Poli et al. 2015, Wang et al. 2019), few accuracy analyses have been performed in areas with large height differences.

In the process of extracting the DEM based on stereo images, the data points collected in the field are divided into two groups: 7 control points and 7 checkpoints. From the accuracy verification of the checkpoints (Table 3), the plane bias and the root mean square error (RMSE) of the seven checkpoints are less than 1 m. In terms of elevation accuracy, the

Table 3 DEM accuracy analysis (bias and root mean squared error are based on GCP (Ground Control Point) measurements)

Point	Co2	Co4	Co6	Co7	C10	C12	C13	Root mean square error
<i>x</i> (m)	0.02	0.49	0.23	-0.64	0.11	-0.68	-0.13	0.4130
<i>y</i> (m)	0.28	-0.36	-0.18	0.75	0.52	0.72	-0.61	0.5296
<i>z</i> (m)	-0.32	0.82	-0.67	1.09	0.94	1.21	-0.72	0.8683

elevation bias of 2 checkpoints is greater than 1 m (1.09 m and 1.21 m) while that of the other five checkpoints is less than 1 m. The bias and RMSE based on GCP measurements clearly show that the planimetric accuracy is better than the vertical accuracy. Similar conclusions have been obtained in previous research (Toutin et al. 2012, Aguilar et al. 2013, Poli et al. 2015). Toutin (Toutin et al. 2012) used 62 independent checkpoints (ICPs) to quantify/validate the accuracy of a DEM based on Worldview-2 imagery. The biases and the standard deviation (Std) of *x*, *y*, and *z* were -0.6 m, 1.7 m, and -2.0 m and 0.34 m, 0.62 m, and 1.54 m, respectively. Aguilar (Aguilar et al. 2013) analyzed orthoimage accuracy using 48 ICPs from WorldView-2 Basic images without control points, and the mean error of *x* and *y* was lower than 0.6 m. Poli (Poli et al. 2015) produced a DEM from Worldview-2 based on seven control points and applied 12 checkpoints to evaluate the DEM accuracy, and the horizontal and vertical RMSE accuracies of *x*, *y*, and *z* were 0.42 m, 0.38 m, and 0.51 m, respectively. The accuracy of *x*, *y*, and *z* in this paper is similar to that of Toutin (Toutin et al. 2012) and worse than that of Aguilar (Aguilar et al. 2013) and Poli (Poli et al. 2015). The data sources and data processing methods in this paper were consistent with those from previous studies that compared data sources and data processing methods. However, the study area characteristics in this paper are different from those of the previous studies. The study area in this paper has a large height difference (1760 m), which is similar to the study area in Toutin (Toutin et al. 2012), which has a height difference of 600 m; therefore, the DEM accuracy of these papers is similar. The study areas in Aguilar (Aguilar et al. 2013) and Poli (Poli et al. 2015) are in flat areas, and these papers have high DEM accuracy. In the distribution of checkpoints, Co7, C10, and C12 are distributed in areas with a large height difference, and their *x*, *y*, and *z* accuracies are relatively low. Moreover, the DEM accuracy is reduced in areas with large height differences. Chaplot (Chaplot et al. 2006) showed that the planimetric and vertical accuracies are low in mountainous areas with steep slopes and large relief amplitudes. The studies from

Fabris (Fabris and Pesci 2005) and Fisher (Fisher and Tate 2006) showed that the accuracy of the DEM is higher in plain areas than in residential areas and lowest in mountainous areas. Therefore, according to the analysis presented here, terrain height differences will affect the accuracy of the extracted DEM and lead to a reduction in DEM accuracy.

4.2 Extraction of DEM from the multiorbit stereo pairs

Due to the limited overlapping area between the multiorbit stereo pairs, there is only one field acquisition control point (C11) and one checkpoint (Co7) in the overlapping area. However, according to previous studies (Cao et al. 2019, Cheng and Chaapel 2008), we can obtain higher positioning accuracy with only 1–2 ground control points. Therefore, we can obtain high DEM accuracy by using one control point.

Based on ERDAS (LPS) software and using a rational function model, the relative orientation and image matching (Wang et al. 2019) were obtained using multitemporal, different-orbit stereo pairs. During the absolute orientation, the same control points (C11) were selected to ensure the accuracy comparison's feasibility and generate an epipolar image. Finally, using bundle-block aerial triangulation, the DEM was acquired (Wang et al. 2019) (Fig. 5).

After obtaining the DEMs of the three experimental schemes, the accuracy of checkpoint Co7 was compared. The biases of *x*, *y*, and *z* in Scheme B were 0.86 m, 1.02 m, 1.67 m, respectively, those in Scheme C were -1.56 m, 1.84 m, and 2.37 m, respectively, and those in Scheme D were 0.98 m, 1.51 m, and 1.94 m, respectively. Although a checkpoint can verify DEM accuracy (Toutin et al. 2012), it was not sufficient to explain the accuracy. We also selected the areas where the three DEMs overlap to carry out the accuracy evaluation. Eighty-one points were uniformly selected as checkpoints in the overlap area, and the analysis was carried out by analyzing the elevation accuracy of Schemes B, C, and D (Fig. 6).

In this paper, the true elevations of the 81 checkpoints were unknown and the factual errors

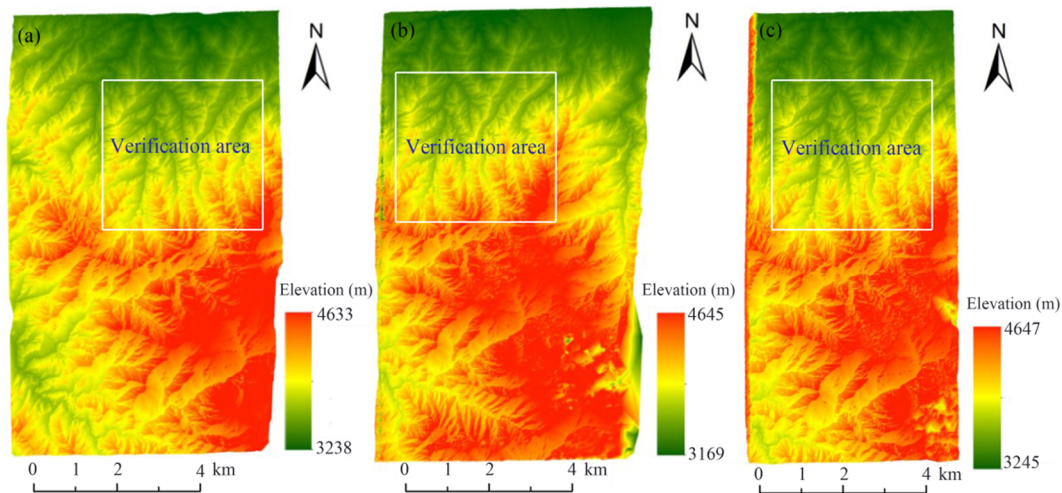


Fig. 5 DEM based on three groups of different experimental data: a) scheme B, b) scheme C, and c) scheme D.

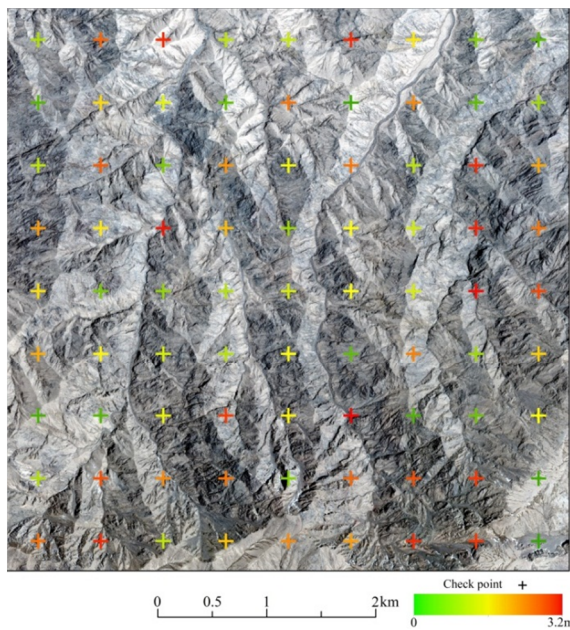


Fig. 6 The distribution of checkpoints and the mean squared error (MSE).

were unknown. Therefore, we used the Bessel formula (Taylor, 1997) to calculate the mean squared error (MSE) (5):

$$\sigma = e\sqrt{\sum_{i=1}^n (y_i - \bar{y})^2 / (n - 1)} \quad (5)$$

where σ is the mean square error, y_i is the measured value, and \bar{y} is the arithmetic mean.

By calculating the mean square error of 81 checkpoints in Schemes B, C, and D, the DEM accuracy from stereo images with different orbits can be analyzed. To more intuitively reflect each control point's medium error distribution, we generated a scatter plot of the medium error distribution (Fig. 6).

The elevation errors of all checkpoints in Schemes B, C, and D were below 3.5 m. Only 12 checkpoints had elevation errors greater than 2 m, and they accounted for 14.8% of the checkpoints. The errors in the other 85.2% of checkpoints were less than 2 m. These results indicate that the accuracy of the DEM extracted from different orbit stereo pairs was relatively stable and reliable.

4.3 Comparison of DEMs generated using different schemes

Because there is only one checkpoint in the DEM range extracted from different track stereo pairs, it is not easy to effectively prove the DEM accuracy. In previous studies, DEMs from LiDAR were often used as the evaluation standard (Aguilar et al. 2013, Poli et al. 2015, Shean et al. 2016, Bagheri et al. 2018). Aguilar (Aguilar et al. 2013) used a very accurate LiDAR-derived DEM (vertical accuracy close to 0.09 m) as a reference to assess the geometric accuracy of the orthorectification process from GeoEye-1 and Worldview-2 panchromatic images. Poli (D. Poli et al. 2015) used a LiDAR DSM as a reference. The height accuracy for the original LiDAR data is given as $rz = 15$ cm for the DSM. Shean (Shean et al. 2016) obtained a DEM from conical-scanning airborne LiDAR, in which the horizontal accuracy was less than 0.75 m and the vertical accuracy was less than 0.1 m. Bagheri (Bagheri et al. 2018) evaluated the success of SAR optical block adjustments with the assistance of available LiDAR point clouds. The planimetric and vertical RMSE values of the LiDAR-derived DEM in two study areas were 1.285 m(x), 1.351 m(y), and

2.653 m(*z*) and 1.566 m(*x*), 1.693 m(*y*), and 3.103 m(*z*). Although LIDAR data in the study area were not obtained in this paper, the DEM was obtained based on the VHR along-track stereo image pair. The DEM accuracy from the along-track image was verified using the field survey control points as checkpoints, and the plane RMSE and elevation RMSE were controlled to within 1 m. Therefore, we used the DEM extracted from along-track satellites in 2015 as the standard DEM to verify the accuracy of the DEM extracted from the multiorbit image. In this study, we compared the overlap region of the four experimental schemes through visual interpretation. The 22 checkpoints were in the same location as in the digital orthophoto map. The plane and elevation coordinates of all 22 checkpoints were acquired. We used the standard DEM (Scheme A) to calculate the errors of scheme B, C, and D. The root mean squared error (RMSE) and mean value of error absolute value (MEAN) were calculated, as shown in Table 4.

In scheme B, most of the absolute values of plane errors (*x* and *y*) were less than 1 m. The elevation errors were slightly larger, with a maximum of -1.99 m. In scheme C, the absolute values of plane errors (*x* and *y*) were all less than 2 m. The absolute plane and elevation errors were slightly higher than those in scheme B, and the elevation errors were also slightly larger, with a

maximum of 2.62 m. In scheme D, the planimetric and vertical accuracy was lower than that of scheme B but higher than that of scheme C. For all schemes, the elevation accuracy was lower than the plane accuracy.

Moreover, the RMSE and MEAN reflected the differences between the three schemes. In scheme B, the plane and elevation RMSEs of *x*, *y*, and *z* were 0.28 m, 0.76 m, and 1.20 m, respectively. In scheme C, the plane and elevation RMSEs of *x*, *y*, and *z* were higher at 1.43 m, 1.30 m, and 1.90 m, respectively. In scheme D, the plane and elevation RMSEs of *x*, *y*, and *z* were 0.97 m, 0.92 m, and 1.48 m, respectively. The MEAN of the three schemes showed the same pattern as the RMSE. The accuracy of the RMSE and MEAN in scheme B was higher than that in scheme D and higher than that in scheme C.

In summary, scheme B showed the highest accuracy and scheme C had higher accuracy than scheme D for *x*, *y*, and *z*. In Schemes B, C, and D, the control points, checkpoints, models and data processing methods were the same and the only difference was the imaging time of the data. The spatial resolution of the data in Schemes B, C, and D was similar, but the off-nadir angles were quite different. The off-nadir angles in 2013, 2014, and 2015 were 18°, 4.9°, and 33.1°, respectively. Theoretically, a larger off-nadir angle corresponds to

Table 4 Absolute errors of checkpoint elevation

Points	Scheme B			Scheme C			Scheme D		
	<i>x</i> (m)	<i>y</i> (m)	<i>z</i> (m)	<i>x</i> (m)	<i>y</i> (m)	<i>z</i> (m)	<i>x</i> (m)	<i>y</i> (m)	<i>z</i> (m)
1	-0.28	0.63	-0.57	1.68	0.31	2.37	-1.06	-0.47	-0.09
2	0.11	1.12	-1.19	1.25	-0.19	-1.36	-1.57	-0.97	0.58
3	0.13	0.13	-1.91	1.11	1.35	-1.59	-0.61	-0.06	1.95
4	0.11	1.14	-1.63	1.88	1.68	-1.23	-0.52	-1.04	0.32
5	0.08	0.66	-1.86	1.67	0.87	-2.02	-1.51	-0.03	1.51
6	0.22	1.15	-1.65	1.23	1.78	1.27	-1.59	-1.06	1.91
7	-0.26	0.66	-1.19	0.75	-0.67	-2.07	-0.13	0.53	1.28
8	-0.38	0.61	-0.62	1.68	0.79	-0.32	-1.55	-1.46	2.27
9	0.21	0.20	0.84	1.21	1.28	-1.33	-1.09	-0.56	0.74
10	-0.34	0.58	-1.99	0.79	0.88	2.81	-0.56	0	1.31
11	0.10	1.19	-0.83	1.79	1.32	-2.15	-1.55	-1.52	1.85
12	0.22	0.67	-0.74	1.21	0.90	-2.35	-0.12	-0.04	1.29
13	0.17	0.64	0.01	1.74	1.32	1.25	-0.59	-1.00	0.50
14	-0.41	0.16	1.34	1.53	1.28	2.33	-0.52	-0.54	0.64
15	-0.34	0.13	-1.75	1.18	1.29	-1.63	-0.57	-0.50	1.75
16	-0.37	0.17	0.32	1.75	1.89	-1.11	-0.53	-0.01	2.48
17	-0.38	0.61	-0.17	1.32	1.40	-2.49	-0.56	-0.49	0.42
18	0.61	1.11	-1.28	1.56	1.87	-2.39	-0.52	-0.98	1.50
19	0.13	0.63	-0.45	1.70	1.77	-0.33	-0.03	-1.46	-0.10
20	0.11	1.06	-1.01	-0.38	1.30	-1.55	-0.95	-0.95	1.93
21	0.19	0.11	-1.29	1.22	1.33	-2.38	-1.53	-1.48	1.22
22	0.17	1.14	-0.19	1.70	1.34	-2.62	-0.57	-1.52	2.47
RMSE	0.28	0.76	1.20	1.43	1.30	1.90	0.97	0.92	1.48
Mean	0.24	0.66	1.04	1.38	1.22	1.77	0.83	0.76	1.28

Note: RMSE = root mean square error.

greater image deformation, which will directly reduce the data processing accuracy. Therefore, the difference between schemes B, C, and D should be caused by the off-nadir angle. Aguilar et al. (Aguilar et al. 2013) showed that off-nadir angles higher than 20° should be avoided; Poli (Poli et al. 2015) demonstrated that the radiometric quality is slightly worse when the off-nadir angle increases; and Shean et al. (Shean et al. 2016) also showed that DEMs acquired with relatively high off-nadir angles displayed high vertical bias.

Although the three schemes' horizontal and vertical accuracies obtained by the three schemes are different, the horizontal errors do not exceed 2 m and the maximum vertical errors do not exceed 3 m. According to the 1:5,000 mapping requirements, the plane error of the digital elevation map (DEM), digital line drawing (DLG), and digital orthophoto map (DOM) must be less than 3.75 m and the elevation error must be less than 6.0 m in high mountain areas. Therefore, the DEM accuracy obtained with the same or different tracks in this paper fully meets the 1:5,000 mapping requirements and thus can meet engineering construction needs.

5 Conclusions

This paper's study area is characterized by high altitude, noticeable terrain elevation differences, and difficulty in obtaining control points and checkpoints in the field. This paper generates a DEM using along-track Worldview-2 stereo imagery and carries out horizontal and vertical accuracy evaluations in areas with high relief degree. Due to the cloud cover of the acquired data in the southeast corner, three different phases were obtained by Worldview-2 imagery, thus forming a stereo image. On this basis, we carried out DEM acquisition and research on the mapping capability of multiorbit and multitemporal stereo pair images. The three main findings can be summarized as follows:

(1) The DEM extracted from the same-orbit WorldView-2 stereo image has high accuracy. The plane and vertical accuracy (RMSE) of this DEM is less than 1 m. However, for the elevation accuracy, the elevation bias of 2 checkpoints is greater than 1 m and reaches 1.09 m and 1.21 m. The bias and RMSE based

on GCP measurements clearly show that the planimetric accuracy is better than the vertical accuracy. According to the accuracy distribution law of 7 checkpoints, the terrain undulations are large and the horizontal and elevation accuracy is reduced.

(2) In the experiment that extracted the DEM from three sets of stereo images, which are composed of three-phase different-orbit images, the median error in the elevation values of 81 checkpoints for the three experimental schemes was distributed below 3.5 m. There were only 12 points with a median elevation error of more than 2 m, and they accounted for 14.8% of the total control points, and the remaining 85.2% had a point error of less than 2 m, indicating that the accuracy of the DEM extracted from the different-orbit stereo image within the same time interval was relatively stable.

(3) The DEM extracted from stereo images uses the 2015 image as the standard of the DEM. Compared to the DEM extracted from the three detournement Worldview-2 stereo images with the standard DEM, we determined that the plane error is less than 2 m and the vertical error is less than 3 m. The difference in precision between the three groups of experimental results shows that the off-nadir angle has a more significant influence on the precision, with a larger off-nadir angle corresponding to greater distortion, which will directly reduce the accuracy of data processing.

In the four sets of DEMs obtained in this paper, the DEM obtained based on 2015 stereo pairs of satellite imagery had the highest precision and contained more GCPs in this application. The data are Stereo1B images, and the model was the RSM. The other three groups of experiments for DEM had low precision, which was because only one GCP was used and the ORS2A image data were processed using the RFM model. The four groups of data acquired to generate the DEM meet the accuracy requirements of a 1:5,000 digital elevation map (DEM), digital line graphic (DLG), and digital orthophoto map (DOM).

Acknowledgement

This research was funded by the Natural Science Foundation of China (No. 41102225, No. 41461021, No. 41661085).

References

- Aguilar MA, Saldaña MM, Aguilar F J (2013) Assessing geometric accuracy of the orthorectification process from GeoEye-1 and Worldview-2 panchromatic images. *Int J Appl Earth Obs Geoinf* 21: 427–435. <https://doi.org/10.1016/j.jag.2012.06.004>
- Akturk E, Altunel A O (2019) Accuracy assessment of a low-cost UAV derived digital elevation model (DEM) in a highly broken and vegetated terrain. *Measurement* 136: 382–386. <https://doi.org/10.1016/j.measurement.2018.12.101>
- Bagheri H, Schmitt M, Angelo P, et al. (2018) A framework for SAR-optical stereogrammetry over urban areas. *ISPRS-J Photogramm Remote Sens* 146: 389–408. <https://doi.org/10.1016/j.isprsjprs.2018.10.003>
- Cao H, Tao P J, Li HH, et al. (2019) Bundle adjustment of satellite images based on an equivalent geometric sensor model with digital elevation model. *ISPRS-J Photogramm Remote Sens* 156: 169–183. <https://doi.org/10.1016/j.isprsjprs.2019.08.011>
- Cheng P, Chaapel C (2008) DigitalGlobe's Worldview-1 satellite: increased image collection opportunities. *Geoinformatics* 16–21.
- Chaplot V, Darboux F, Bourennane H, et al. (2006) Accuracy of interpolation techniques for the derivation of digital elevation models in relation to landform types and data density. *Geomorphology* 77(1–2): 126–141. <https://doi.org/10.1016/j.geomorph.2005.12.010>
- DigitalGlobe Inc (2010) DigitalGlobe Core Imagery Products Guide. http://www.digitalglobe.com/downloads/DigitalGlobe_Core_Imagery_Products_Guide.pdf (Accessed on January 5, 2020)
- DigitalGlobe (2020) <http://www.digitalglobe.com/resources#resource-table-section> (Accessed on January 5, 2020)
- Fabris M, Pesci A (2005) Automated DEM extraction in digital aerial photogrammetry: precisions and validation for mass movement monitoring. *Ann Geophys* 48(6): 57–72. <https://doi.org/10.4401/ag-3247>
- Fraser CS, Baltasvias E, Gruen A (2002a) Processing of IKONOS imagery for submetre 3D geopositioning and building extraction. *ISPRS-J Photogramm Remote Sens* 56(3): 177–194. [https://doi.org/10.1016/S0924-2716\(02\)00045-X](https://doi.org/10.1016/S0924-2716(02)00045-X)
- Fisher PF, Tate NJ (2006) Causes and consequences of error in digital elevation models. *Prog Phys Geog* 30(4): 467–489. <https://journals.sagepub.com/doi/10.1191/0309133306pp492ra>
- Fraser CS, Hanley H, Yamakawa T (2002b) Three-dimensional geopositioning accuracy of IKONOS imagery. *Photogramm Rec* 17(99): 465–480. <https://doi.org/10.1111/0031-868X.00199>
- Fraser CS, Ravanbakhsh M (2009) Georeferencing accuracy of GeoEye-1 imagery. *Photogramm Eng Remote Sens* 75(6): 634–640. <https://doi.org/10.1111/j.1435-5957.2009.00246.x>
- Giribabu D, Rao SS, Murthy Krishna YVN (2013) Improving Cartosat-1 DEM accuracy using synthetic stereo pair and triplet. *ISPRS-J Photogramm Remote Sens* 77: 31–43. <https://doi.org/10.1016/j.isprsjprs.2012.12.005>
- Gouldena T, Hopkinson C, Jamieson R, et al. (2016) Sensitivity of DEM, slope, aspect and watershed attributes to LiDAR measurement uncertainty. *Remote Sens Environ* 179: 23–35. <https://doi.org/10.1016/j.rse.2016.03.005>
- Goldbergs G, Maier SW, Levick SR, et al. (2019) Limitations of high resolution satellite stereo imagery for estimating canopy height in Australian tropical savannas. *Int J Appl Earth Obs Geoinformation* 75: 83–95. <https://doi.org/10.1016/j.jag.2018.10.021>
- In K, Jeong S, Kim KO, et al. (2003) Automatic DEM generation using IKONOS stereo imagery. In: *Geoscience and Remote Sensing Symposium, IGARSS '03, Proceedings, 2003 IEEE, International 7*: 4289–4291. <https://doi.org/10.1109/IGARSS.2003.1295492>
- Jeong J, Kim T (2015) Comparison of positioning accuracy of a rigorous sensor model and two rational function models for weak stereo geometry. *ISPRS-J Photogramm Remote Sens* 108: 172–182. <https://doi.org/10.1016/j.isprsjprs.2015.07.006>
- Lacroix P, Berthier E, Maquerhua ET (2015) Earthquake-driven acceleration of slow-moving landslides in the Colca valley, Peru, detected from Pleiades images. *Remote Sens Environ* 165: 148–158. <https://doi.org/10.1016/j.rse.2015.05.010>
- Muskett RR, Lingle CS, Sauber JM, et al. (2008) Acceleration of surface lowering on the tidewater glaciers of Icy Bay, Alaska, U.S.A. from InSAR DEMs and ICESat altimetry. *Earth Planet Sci Lett* 265: 345–359. <https://doi.org/10.1016/j.epsl.2007.10.012>
- Nemmaoui A, Aguilar FJ, Aguilar Manuel A, et al. (2019) DSM and DTM generation from VHR satellite stereo imagery over plastic covered greenhouse areas. *Comput Electron Agric* 164: 104903. <https://doi.org/10.1016/j.compag.2019.104903>
- Noguchi M, Fraser CS, Nakamura T, et al. (2004) Accuracy assessment of QuickBird stereo imagery. *Photogramm Rec* 19(106): 128–137. <https://doi.org/10.1111/j.1477-9730.2004.00035.x>
- Noh MJ, Howat IM (2015) Automated stereo-photogrammetric DEM generation at high latitudes: Surface Extraction with TIN-based Search-space Minimization (SETISM) validation and demonstration over glaciated regions. *GISci. Remote Sens* 52: 198–217. <https://doi.org/10.1080/15481603.2015.1008621>
- Poli D, Toutin T (2012) Review of developments in geometric modelling for high resolution satellite pushbroom sensors. *Photogramm Rec* 27(137): 58–73. <https://doi.org/10.1111/j.1477-9730.2011.00665.x>
- Poli D, Remondino F, Angiuli E, et al. (2015) Radiometric and geometric evaluation of GeoEye-1, Worldview-2 and Pleiades-1A stereo images for 3D information extraction. *ISPRS-J Photogramm Remote Sens* 100: 35–47. <https://doi.org/10.1016/j.isprsjprs.2014.04.007>
- Reinartz P, Tian J, Arefi H, et al. (2014) Advances in DSM generation and higher level information extraction from high resolution optical stereo satellite data. In: *34th Earsel Symposium, European Remote Sensing - New Opportunities for Science and Practice*. p. 10 pages (on CD-ROM). <https://doi.org/10.12760/03-2014-21>
- Saldaña MM, Aguilar MA, Aguilar FJ, et al. (2012) DSM extraction and evaluation from GeoEye-1 stereo imagery, XXII Congress of the International Society for Photogrammetry and Remote Sensing. 113–118. <https://doi.org/10.5194/isprannals-1-4-113-2012>
- Shaker A, Yan WY, Easa S (2010) Using stereo satellite imagery for topographic and transportation applications: an accuracy assessment. *Geosci Remote Sens* 47(3): 321–337. <https://doi.org/10.2747/1548-1603.47.3.321>
- Shean DE, Alexandrov O, Moratto ZM, et al. (2016) An automated, open-source pipeline for mass production of digital elevation models (DEMs) from very-high-resolution commercial stereo satellite imagery. *ISPRS-J Photogramm Remote Sens* 116: 101–117. <https://doi.org/10.1016/j.isprsjprs.2016.03.012>
- Taylor JR (1997) *An introduction to error analysis*. University Sciences Books, Sausalito, California.
- Toutin T, Cheng P (2001) DEM Generation with ASTER stereo data. *Earth Observation Magazine* 10(6): 10–13.
- Toutin T (2004) Comparison of stereo-extracted DTM from different high-resolution sensors: SPOT-5, EROS-A, IKONOS-II, and Quick Bird. *IEEE Trans. Geosci Remote Sensing* 42(10): 2121–2129. <https://doi.org/10.1109/TGRS.2004.834641>
- Toutin T (2011) State-of-the-art of geometric correction of remote sensing data: a data fusion perspective. *Int J Image Data Fus* 2(1): 3–35. <https://doi.org/10.1080/19479832.2010.539188>
- Toutin T, Schmitt C V, Wang H (2012) Impact of no GCP on elevation extraction from World View stereo data. *ISPRS-J Photogramm Remote Sens* 72: 73–79. <http://doi.org/10.1016/j.isprsjprs.2012.05.009>
- Uysal M, Toprak AS, Polat N (2015) DEM generation with UAV Photogrammetry and accuracy analysis in Sahitler hill. *Measurement* 73: 539–543. <https://doi.org/10.1016/j.measurement.2015.06.010>
- Vassilaki DI, Stamos AA (2020) TanDEM-X DEM: Comparative performance review employing LIDAR data and DSMs. *ISPRS-J Photogramm Remote Sens* 160: 33–50. <https://doi.org/10.1016/j.isprsjprs.2019.11.015>
- Wang SY, Ren ZK, Wu CY, et al. (2019) DEM generation from Worldview-2 stereo imagery and vertical accuracy assessment for its application in active tectonics. *Geomorphology* 336(2019): 107–118. <https://doi.org/10.1016/j.geomorph.2019.03.016>
- Zhang L, Gruen A (2006) Multi-image matching for DSM generation from Ikonos imagery. *ISPRS-J Photogramm Remote Sens* 60(3): 195–211. <https://doi.org/10.1016/j.isprsjprs.2006.01.001>
- Zhu XX, Baier G, Lachaise M, et al. (2018) Potential and limits of non-local means InSAR filtering for TanDEM-X high-resolution DEM generation. *Remote Sens Environ* 218: 148–161. <https://doi.org/10.1016/j.rse.2018.09.012>
- Zhou Y, Parsons B, Elliott JR, et al. (2015) Assessing the ability of Pleiades stereo imagery to determine height changes in earthquakes: a case study for the El Mayor-Cuapah epicentral area. *J. Geophys. Res. Solid Earth* 120(12): 8793–8808.